

OctreeOcc: Efficient and Multi-Granularity Occupancy Prediction Using Octree Queries

Yuhang Lu¹, Xinge Zhu², Tai Wang^{3,†}, and Yuexin Ma^{1,†}

¹ ShanghaiTech University

² The Chinese University of Hong Kong

³ Shanghai AI Laboratory

{luyh2,mayuexin}@shanghaitech.edu.cn, taiwang.me@gmail.com

Abstract. Occupancy prediction has increasingly garnered attention in recent years for its fine-grained understanding of 3D scenes. Traditional approaches typically rely on dense, regular grid representations, which often leads to excessive computational demands and a loss of spatial details for small objects. This paper introduces OctreeOcc, an innovative 3D occupancy prediction framework that leverages the octree representation to adaptively capture valuable information in 3D, offering variable granularity to accommodate object shapes and semantic regions of varying sizes and complexities. In particular, we incorporate image semantic information to improve the accuracy of initial octree structures and design an effective rectification mechanism to refine the octree structure iteratively. Our extensive evaluations show that OctreeOcc not only surpasses state-of-the-art methods in occupancy prediction, but also achieves a 15% – 24% reduction in computational overhead compared to dense-grid-based methods.

Keywords: 3D Scene Understanding · Occupancy Prediction · Octree

1 Introduction

Holistic 3D scene understanding is a pivotal aspect of a stable and reliable visual perception system, especially for real-world applications such as autonomous driving. Occupancy, as a classical representation, has been reascent recently with more datasets support and exploration in learning-based approaches. Such occupancy prediction tasks aim at partitioning the 3D scene into grid cells and predicting semantic labels for each voxel. It is particularly an essential solution for recognizing irregularly shaped objects and also enables the open-set understanding [40], further benefiting downstream tasks, like prediction and planning.

Existing occupancy prediction methods [9, 12, 22, 51, 56] typically construct dense and regular grid representations, same as the ground truth. While such approach is intuitive and direct, it overlooks the statistical and geometric properties of 3D environments. In fact, the 3D scene is composed of foreground objects

[†] Corresponding authors

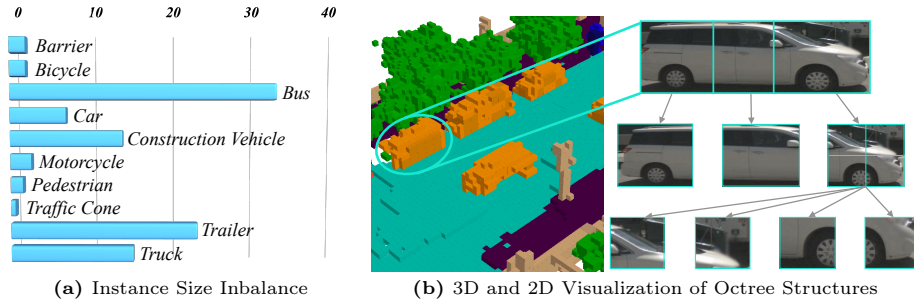


Fig. 1: Scale difference of various categories and octree representation. (a) presents a comparison of the average space occupied by each type of object, indicating different granularities are required for different semantic regions. (b) shows the superiority of octree representations, where we can apply specific granularity not only for different objects but also for different parts of the object, which can reduce computational overhead while preserving spatial information.

and background regions with various shapes and sizes. For example, the space occupied by larger objects, such as buses, are considerably more extensive than that taken up by smaller items like traffic cones (Fig. 1a). Consequently, employing a uniform voxel resolution to depict the scene proves to be inefficient, leading to computational waste for larger objects and a lack of geometry details for smaller ones. Considering the large computation cost of aforementioned works, some recent works attempted to mitigate the heavy memory footprint by utilizing other representations, such as 2D planes in TPVFormer [11] and coarse voxels in PanoOcc [50], or modeling non-empty regions by depth estimation [18]. However, these methods suffer from the loss of spatial information because of too coarse representations or accumulated estimated depth errors.

To reduce the computational overhead and meanwhile improve the prediction accuracy, we propose to use octree [29] representation for the occupancy prediction, which can flexibly adapt to objects and semantic regions with various shapes and sizes. As a tree-based data structure, it recursively divides the 3D space into eight octants, thus allowing coarse spatial partition for large regions and fine-grained processing for small objects or complex details (Fig. 1b). Incorporating octree representation, we propose *OctreeOcc*, an efficient and multi-granularity method for occupancy prediction. It constructs octree queries by predicting the octree structure from the stored features of leaf nodes at each level of the tree. However, directly predicting 3D structure from 2D images is challenging due to the lack of depth and occlusion issues. To address this problem, we first propose **Semantic-guided Octree Initialization** that incorporates image semantic information to produce more accurate initial structures. And then, we devise an **Iterative Structure Rectification** module that predicts new octree structure from the encoded query to rectify the low-confidence region of the original prediction, further improving the prediction precision.

Our extensive evaluations against state-of-the-art occupancy prediction methods show that *OctreeOcc* outperforms others on nuScenes and SemanticKITTI

datasets, reducing computational overhead by 15% – 24% for dense-grid-based methods. Ablation studies further validate the effectiveness of each module within our method. Our contributions can be summarized as follows:

- We introduce *OctreeOcc*, a 3D occupancy prediction approach based on multi-granularity octree queries. This method facilitates spatial sparsification, significantly decreasing the number of voxels needed to accurately depict a scene, yet retains critical spatial details.
- We propose a semantic-guided octree initialization module and an iterative structure rectification module. These enhancements empower the network with a robust initial setup and the ability to dynamically refine the octree, leading to a more efficient and effective representation.
- Comprehensive experiments demonstrate that OctreeOcc achieves state-of-the-art performance and reduces computational overhead, highlighting the feasibility and potential of octree structures in 3D occupancy prediction.

2 Related Work

2.1 Camera-based 3D Perception

Camera-based 3D perception has gained significant traction in recent years due to its ease of deployment, cost-effectiveness, and the preservation of intricate visual attributes. According to the view transformation paradigm, these methods can be categorized into three distinct types. LSS-based approaches [9, 19, 20, 27, 33, 34] explicitly lift multi-view image features into 3D space through depth prediction. Another category of works [13, 21, 53] implicitly derives depth information by querying from 3D to 2D. Notably, projection-free methods [24–26, 48] have recently demonstrated exceptional performance. While commendable progress has been made in detection, this approach compromises the comprehensive representation of the overall scene in 3D space and proves less effective in recognizing irregularly shaped objects. Consequently, there is a burgeoning interest in methodologies aimed at acquiring a dense voxel representation through the camera, facilitating a more comprehensive understanding of 3D space.

2.2 3D Occupancy Prediction

3D occupancy prediction involves the prediction of both occupancy and semantic attributes for all voxels encompassed within a three-dimensional scene, particularly valuable for autonomous vehicular navigation. Recently, some valuable datasets [39, 43, 49] have been proposed, boosting more and more research works [3, 10–12, 18, 28, 30–32, 38, 40, 50, 51, 54–56] in this field. Most of the research in occupancy prediction focuses on dense voxel modeling. MonoScene [3] pioneers a camera-based approach using a 3D UNet architecture. OccDepth [30] improves 2D-to-3D geometric projection using stereo-depth information. OccFormer [56] decomposes the 3D processing into the local and global transformer pathways along the horizontal plane. SurroundOcc [51] achieves fine-grained results with

multiscale supervision. Symphonies [12] introduces instance queries to enhance scene representation.

Nevertheless, owing to the high resolution of regular voxel representation and sparse context distribution in 3D scenes, these methods encounter substantial computational overhead and efficiency issues. Some approaches recognize this problem and attempt to address it by reducing the number of modeled voxels. For instance, TPVFormer [11] employs a strategy of modeling the three-view 2D planes and subsequently recovering 3D spatial information from them. However, its performance degrades due to the lack of 3D information. PanoOcc [50] initially represents scenes at the coarse-grained level and then upsamples them to the fine-grained level, but the lack of information from coarse-grained modeling cannot be adequately addressed by the up-sampling process. VoxFormer [18] mitigates computational complexity by initially identifying non-empty regions through depth estimation and modeling only those specific areas. However, the effectiveness of this process is heavily contingent on the accuracy of depth estimation. In contrast, our approach provides different granularity of modeling for different regions by predicting the octree structure, which reduces the number of voxels to be modeled while preserving the spatial information, thereby reducing the computational overhead and maintaining the prediction accuracy.

2.3 Octree-Based 3D Representation

The octree structure [29] has been widely used in the field of computer graphics to boost the process of rendering or reconstruction [7, 15, 41, 46]. Due to its spatial efficiency and ease of implementation on GPU architectures, researchers have also applied octrees in efficient point cloud learning and various related works [16, 42, 45, 47]. OctFormer [44] and OcTr [57] utilize multi-granularity features of octree to capture a comprehensive global context, thereby enhancing the efficiency of understanding point clouds at the scene level. Furthermore, certain studies [6, 35] adopt octree representation for effectively compressing point cloud data. These works have highlighted the versatility and effectiveness of octree-based methodologies in point cloud analysis and processing applications. However, unlike constructing an octree from 3D point clouds, we are the first to predict the octree structure of a 3D scene from images, which is more challenging owing to the absence of explicit spatial information inherent in 2D images.

3 Methodology

In this section, we introduce details of our efficient and multi-granularity occupancy prediction method *OctreeOcc*. After defining the problem and providing an overview of our method in Sec. 3.1 and 3.2, we introduce key components of our method in order. In Sec. 3.3, we outline how we define octree queries and transform dense queries into octree queries. Next, we utilize image semantic priors to construct a high-quality initialized octree structure, as detailed in Sec. 3.4. Once the initialized octree query is obtained, we encode it and refine the octree

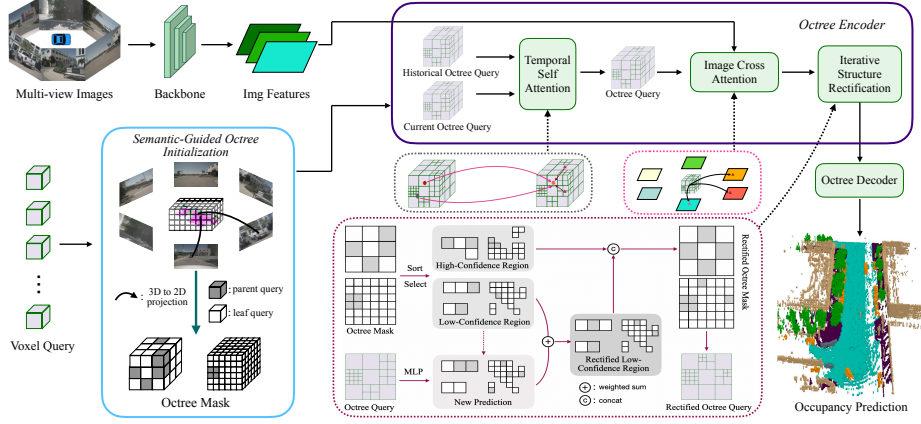


Fig. 2: Overall framework of OctreeOcc. Given multi-view images, we extract multi-scale image features utilizing an image backbone. Subsequently, the initial octree structure is derived through image segmentation priors, and the transformation of dense queries into octree queries is effected. Following this, we concomitantly refine octree queries and rectify the octree structure through the octree encoder. Finally, we decode from the octree query and obtain occupancy prediction outcomes for this frame. For better visualisation, the diagram of Iterative Structure Rectification module shows octree query and mask in 2D form(quadtree).

structure in Sec. 3.5. Finally, Sec. 3.6 and 3.7 describe the process of generating octree ground truth and how to supervise the network, respectively.

3.1 Problem Setup

Camera-based occupancy prediction aims to predict the present occupancy state and semantics of each voxel grid within the scene using input from multi-view camera images. Specifically, we consider a set of N multi-view images $I = \{I_i \in \mathbb{R}^{H \times W \times 3}\}_{i=1}^N$, together with camera intrinsics $K = \{K_i \in \mathbb{R}^{3 \times 3}\}_{i=1}^N$ and extrinsics $T = \{T_i \in \mathbb{R}^{4 \times 4}\}_{i=1}^N$ as input, and the objective of the model is to predict the 3D semantic voxel volume $O \in \{w_0, w_1, \dots, w_C\}^{X \times Y \times Z}$, where H, W indicate the resolution of input image and X, Y, Z denote the volume resolution (e.g. $200 \times 200 \times 16$). The primary focus lies in accurately distinguishing the empty class (w_0) and other semantic classes ($w_1 \sim w_C$) for every position in the 3D space, which entails the network learning both the geometric and semantic information inherent in the data.

3.2 Overview

Given a set of multi-view images $I = \{I_i \in \mathbb{R}^{H \times W \times 3}\}_{i=1}^N$, we extract multi-view image features $\mathbb{F} = \{F_i \in \mathbb{R}^{H \times W \times C}\}_{i=1}^N$. Simultaneously, we initialize the dense voxel query $Q_{dense} \in \mathbb{R}^{X \times Y \times Z \times C}$. To enhance computational efficiency,

we transform Q_{dense} into sparse representation $Q_{octree} \in \mathbb{R}^{N \times C}$, leveraging octree structure information (*i.e.* octree mask) derived from segmentation priors. During encoding, we utilize Q_{octree} to gather information, including temporal fusion and sampling from image features \mathbb{F} , while also rectifying the octree structure. Upon encoding Q_{octree} , to conform to the output format, we convert it back to Q_{dense} and apply a Multi-Layer Perceptron (MLP) to obtain the final occupancy prediction $O \in \mathbb{R}^{X \times Y \times Z \times K}$. Here, H, W indicate the resolution of input image and X, Y, Z denote the volume resolution. N means the number of octree query, C denotes the feature dimension and K indicates the number of classes.

3.3 Octree Query

Given that objects within 3D scenes exhibit diverse granularities, employing dense queries [51, 56] overlooks this variation and leads to inefficiency. To address this, we propose sparse and multi-granularity octree queries, leveraging the octree structure. This approach creates adaptable voxel representations tailored to semantic regions at different scales.

Octree Mask. To effectively construct the octree query, it’s essential to understand its underlying structure. An octree partitions each node into eight child nodes within 3D space, each representing equal subdivisions of the parent node. This recursive process begins with the initial level and proceeds with gradual splitting. At every level, a voxel query serves either as a leaf query if it remains unsplit or as a parent query if it undergoes division. We obtain this geometric information by maintaining a learnable octree mask, denoting as $M_o = \{M_o^l \in \mathbb{R}^{\frac{X}{2^l}, \frac{Y}{2^l}, \frac{Z}{2^l}}\}_{l=1}^{L-1}$, where X, Y, Z denote the ground truth’s volume resolution. The L denotes the depth of the octree, representing the existence of L different resolutions of queries, with $L - 1$ splits being performed from the top to the bottom of the octree. The value in the octree mask represents the probability that a voxel at that level requires a split, which is initialized through segmentation priors (Sec. 3.4), rectified during query encoding (Sec. 3.5), and supervised by octree ground truth (Sec. 3.7).

Transformation between octree query and dense voxel query. During the query encoding process, we prioritize efficiency by leveraging octree queries. This involves transforming the initial dense queries Q_{dense} into octree queries Q_{octree} using learned structural information. To determine the octree structure, we need to binarise the learned octree mask. Due to the fact that most of the voxels in the scene at various resolutions do not necessitate splitting, neural network-based prediction binarization is susceptible to pattern collapse, tending to predict all as non-split, leading to a decrease in performance. To mitigate this issue, we introduce a manually defined query selection ratio, where a subset of voxels with the highest probability of splitting is selected for division through the top-k mechanism.

The transformation from Q_{dense} to Q_{octree} begins at the finest granularity, we downsample Q_{dense} to each level through average pooling and retain queries that do not require splitting (leaf queries) with the assistance of the binarized octree

mask. This process iterates until reaching the top of the octree. By retaining all leaf queries, we establish $Q_{octree} \in \mathbb{R}^{N \times C}$, where $N = N_1 + N_2 + \dots + N_L$ represents the total count of leaf queries, L indicates the depth of octree. Conversely, applying the inverse operation of this process allows the conversion of Q_{octree} back into Q_{dense} for the final output. Further details are provided in Supplementary.

3.4 Semantic-Guided Octree Initialization

Predicting octree structure from an initialised query via neural network can yield sub-optimal results due to the inherent lack of meaningful information in the query. To overcome this limitation, we employ the semantic priors inherent in images as crucial references. Specifically, we adopt UNet [37] to segment the input multi-view images I and obtain the segment map $I_{seg} = \{I_{seg}^i \in \mathbb{R}^{H \times W}\}_{i=1}^N$. We then generate sampling points $p = \{p_i \in \mathbb{R}^3\}_{i=1}^{X \times Y \times Z}$, with each point corresponding to the center coordinates of dense voxel queries. Subsequently, we project these points onto various image views. The projection from sampling point $p_i = (x_i, y_i, z_i)$ to its corresponding 2D reference point (u_{ij}, v_{ij}) on the j -th image view is formulated as:

$$\pi_j(p_i) = (u_{ij}, v_{ij}), \quad (1)$$

where $\pi_j(p_i)$ denotes the projection of the i -th sampling point at location p_i on the j -th camera view. We project the point p_i onto the acquired semantic segmentation map I_{seg} through the described projection process. To prioritize effective areas like foreground objects and buildings in the initial structure, we employ an unbalanced assignment approach, where the highest weight is assigned to voxels projecting to foreground areas, followed by lesser weights for voxels projecting to buildings or vegetation, and the least weight for voxels projecting to roads, etc.

During this process, we determine the weights of each voxel at the finest granularity, denoted as $W \in \mathbb{R}^{X \times Y \times Z}$. Subsequently, we employ average pooling to downsample W to each level of the octree, resulting in an initial octree mask $M_o = \{M_o^l \in \mathbb{R}^{\frac{X}{2^l}, \frac{Y}{2^l}, \frac{Z}{2^l}}\}_{l=1}^{L-1}$. Here, X , Y , and Z represent the resolution of the ground truth volume, while L denotes the depth of the octree. Further details are provided in the Supplementary.

3.5 Octree Encoder

Given octree queries Q_{octree} and extracted image features \mathbb{F} , the octree encoder updates both the octree query features and the octree structure. Referring to the querying paradigm in dense query-based methods [39, 50], we adopt efficient deformable attention [59] for temporal self-attention(TSA) and image cross-attention(ICA).

In accurately representing the driving scene, temporal information plays a crucial role. By leveraging historical octree queries Q_{t-1} , we align it to the

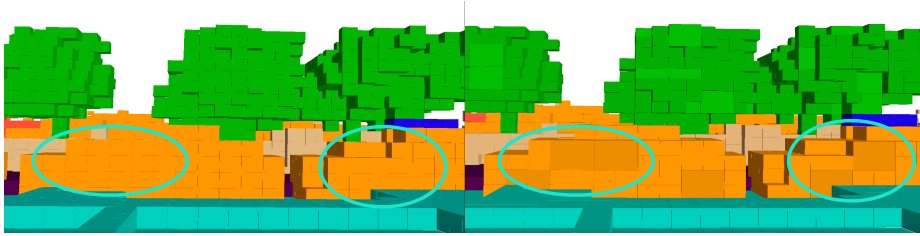


Fig. 3: Illustration of octree structure rectification. The left figure displays the initially predicted octree structure and the right figure depicts the octree structure after Iterative Structure Rectification. It is evident that the predicted octree structure becomes more consistent with the object’s shape following the rectification module.

current octree queries by the ego-vehicle motion transformation. Given historical octree queries $Q_{t-1} \in \mathbb{R}^{N,C}$, a current octree query q located at $p = (x, y, z)$, the TSA is represented by:

$$TSA(q, Q_{t-1}) = \sum_{m=1}^{M_1} DeformAttn(q, p, Q_{t-1}), \quad (2)$$

where M_1 indicates the number of sampling points. Implementing it within the voxel-based self-attention ensures that each octree query interacts exclusively with local voxels of interest, keeping the computational cost manageable.

Image cross-attention is devised to enhance the interaction between multi-scale image features and octree queries. Specifically, for an octree query q , we can obtain its centre’s 3D coordinate (x, y, z) as reference point $Ref_{x,y,z}$. Then we project the 3D point to images like formula 1 and perform deformable attention:

$$ICA(q, \mathbf{F}) = \frac{1}{N} \sum_{n \in N} \sum_{m=1}^{M_2} DeformAttn(q, \pi_n(Ref_{x,y,z}), \mathbf{F}_n), \quad (3)$$

where N denotes the camera view, m indexes the reference points, and M_2 is the total number of sampling points for each query. \mathbf{F}_n is the image features of the n -th camera view.

Iterative Structure Rectification Module. The initial octree structure is derived from information obtained through image segmentation, but it may not precisely correspond to the actual scene due to potential segmentation and projection errors. Nonetheless, the encoded octree query captures crucial spatial information. Thus, the predicted octree structure based on this query complements and rectifies the initial structure prediction, allowing us to mitigate limitations arising from segmentation and projection issues.

Specifically, we partition the octree structure into two parts: the high-confidence regions and the low-confidence regions, as Fig. 2 shows. By sorting the octree split probability values stored in the octree mask in descending order and selecting the top $k\%$ of regions at each level, we can identify the locations of

high-confidence regions. For these regions, predictions are relatively more accurate and no additional adjustments are required in this iteration. For regions where confidence remains low, we first extract the query features corresponding to those areas by utilizing the index of low-confidence regions, denoted as $Q_{lcr} = \{Q_{lcr}^l \in \mathbb{R}^{N_l \times C}\}_{l=1}^{L-1}$, where N_l represents the number of low-confidence queries in level l . We then employ a Multi-layer Perceptron (MLP) to predict octree split probabilities from Q_{lcr} . Subsequently, we apply a weighted sum with the previous split probability predictions of low-confidence regions to obtain rectified predictions. These refined predictions are concatenated with the preserved probability predictions of high-confidence regions, culminating in the generation of the final rectified octree mask. More details are shown in Supplementary.

It is worth noting that, due to the iterative nature of structure updates, regions initially considered high confidence may not necessarily remain unchanged, as they might be partitioned into low-confidence regions in the next iteration.

3.6 Octree Ground Truth Generation

We derive the octree ground truth from the semantic occupancy ground truth. Specifically, for a voxel at level l in the octree, we identify its corresponding 8^{L-l} voxels in the semantic occupancy ground truth. If these voxels share the same labels, we deem the voxel at level l unnecessary to split (assigned a value of 0); otherwise, it necessitates division (assigned a value of 1), as the current resolution is insufficient to represent it adequately. Through this process, each voxel at each level is assigned a binary value of 0 or 1. Then we obtain the octree ground truth $G_{octree} = \{G_{octree}^l \in \mathbb{R}^{\frac{X}{2^l}, \frac{Y}{2^l}, \frac{Z}{2^l}}\}_{l=1}^{L-1}$. Here, L represents the depth of the octree, while X , Y , and Z denote the volume resolution of the semantic occupancy ground truth. G_{octree} is employed to supervise the octree mask using focal loss, facilitating the network in learning the octree structure information.

3.7 Loss Function

To train the model, we use focal loss L_{focal} , lovasz-softmax loss L_{ls} , dice loss L_{dice} , affinity loss L_{scal}^{geo} and L_{scal}^{sem} from MonoScene [3]. In addition, we also use focal loss to supervise the octree prediction. The overall loss function $L = L_{focal} + L_{ls} + L_{dice} + L_{scal}^{geo} + L_{scal}^{sem} + L_{octree}$.

4 Experiments

In this section, we commence by introducing the datasets (Sec. 4.1), evaluation metrics (Sec. 4.2), and implementation details (Sec. 4.3). Subsequently, we evaluate our method on 3D occupancy prediction and semantic scene completion tasks (Sec. 4.4) to demonstrate its effectiveness. Additionally, we conduct ablation studies (Sec. 4.5) and provide more analysis (Sec. 4.6) of our method to validate its efficacy and superiority.

4.1 Datasets

Occ3D-nuScenes [43] constitutes a re-annotation of the nuScenes dataset [2], where precise ground truth labels for occupancy have been derived by aggregating LiDAR scans and human annotations. These annotations adhere to the ego coordinate system framework, consisting of 700 instances for training and 150 for validation. The spatial extents of occupancy along the X and Y axes in ego-coordinates are limited to the range of -40 meters to 40 meters, while the Z-axis spans from -1 meter to 5.4 meters. The occupancy labels are categorized into 17 distinct classes, with each class representing a volumetric space of 0.4 meters in each dimension ($0.4\text{m} \times 0.4\text{m} \times 0.4\text{m}$). Additionally, the dataset includes semantic labeling for the 18th category, denoted as "free", which represents the empty regions within a scene. Finally, Occ3D-nuScenes provides visibility masks for both LIDAR and camera modalities.

SemanticKITTI [1] comprises 22 distinct outdoor driving scenarios, with a focus on areas located in the forward trajectory of the vehicle. Each sample in this dataset covers a spatial extent ranging from $[0.0\text{m}, -25.6\text{m}, -2.0\text{m}, 51.2\text{m}, 25.6\text{m}, 4.4\text{m}]$, with a voxel granularity set at $[0.2\text{m}, 0.2\text{m}, 0.2\text{m}]$. The dataset consists of volumetric representations, specifically in the form of $256 \times 256 \times 32$ voxel grids. These grids undergo meticulous annotation with 21 distinct semantic classes. The voxel data is derived through a rigorous post-processing procedure applied to Lidar scans.

4.2 Evaluation metrics

Both 3D occupancy prediction and semantic scene completion utilize intersection-over-union (mIoU) over all classes as evaluation metrics, calculated as follows:

$$\text{mIoU} = \frac{1}{C} \sum_{c=1}^C \frac{\text{TP}_c}{\text{TP}_c + \text{FP}_c + \text{FN}_c}, \quad (4)$$

where TP_c , FP_c , and FN_c correspond to the number of true positive, false positive, and false negative predictions for class c_i , and C is the number of classes.

4.3 Implementation Details

Based on previous research, we set the input image size to 900×1600 and employ ResNet101-DCN [5] as the image backbone. Multi-scale features are extracted from the Feature Pyramid Network (FPN) [23] with downsampling sizes of $1/8$, $1/16$, $1/32$, and $1/64$. The feature dimension C is set to 256. The octree depth is 3, and the initial query resolution is $50 \times 50 \times 4$. We choose query selection ratios of 20% and 60% for the two divisions. The octree encoder comprises three layers, each composed of Temporal Self-Attention (TSA), Image Cross-Attention (ICA), and Iterative Structure Rectification (ISR) modules. Both M_1 and M_2 are set to 4. In ISR, the top 10% predictions are considered high-confidence in level 1, and 30% in level 2. The loss weights are uniformly set to 1.0. For optimization,

Table 1: 3D Occupancy prediction performance on Occ3D-nuScenes dataset. “★” denotes training with the camera mask.

Method	Image Backbone	Reference	mIoU	others	barrier	bicycle	bus	car	const. veh.	motorcycle	pedestrian	traffic cone	trailer	truck	drive. suf.	other flat	sidewalk	terrain	manmade	vegetation
MonoScene [3]	ResNet101	CVPR’22	6.06	1.75	7.23	4.26	4.93	9.38	5.67	3.98	3.01	5.90	4.45	7.17	14.91	6.32	7.92	7.43	1.01	7.65
BEVDet [9]	ResNet101	arxiv’21	11.73	2.09	15.29	0.0	4.18	12.97	1.35	0.0	0.43	0.13	6.59	6.66	52.72	19.04	26.45	21.78	14.51	15.26
BEVFormer [21]	ResNet101	ECCV’22	23.67	5.03	38.79	9.98	34.41	41.09	13.24	16.50	18.15	17.83	18.66	27.70	48.95	27.73	29.08	25.38	15.41	14.46
BEVStereo [19]	ResNet101	AAAI’23	24.51	5.73	38.41	7.88	38.70	41.20	17.56	17.33	14.69	10.31	16.84	29.62	54.08	28.92	32.68	26.54	18.74	17.49
TPVFormer [11]	ResNet101	CVPR’23	28.34	6.67	39.20	14.24	41.54	46.98	19.21	22.64	17.87	14.54	30.20	35.51	56.18	33.65	35.69	31.61	19.97	16.12
OccFormer [50]	ResNet101	ICCV’23	21.93	5.94	30.29	12.32	34.40	39.17	14.44	16.45	17.22	9.27	13.90	26.36	50.99	30.96	34.66	22.73	6.76	6.97
CTF-Occ [43]	ResNet101	NeurIPS’23	28.53	8.09	39.33	20.56	38.29	42.24	16.93	24.52	22.72	21.05	22.98	31.11	53.33	33.84	37.98	33.23	20.79	18.00
RenderOcc [32]	ResNet101	ICRA’24	26.11	4.84	31.72	10.72	27.67	26.45	13.87	18.2	17.67	17.84	21.19	23.25	63.20	36.42	46.21	44.26	19.58	20.72
BEVDet4D [8]★	Swin-B	arxiv’22	42.02	12.15	49.63	25.1	52.02	54.46	27.87	27.99	28.94	27.23	36.43	42.22	82.31	43.29	54.46	57.9	48.61	43.55
PanoOcc [50]★	ResNet101	CVPR’24	42.13	11.67	50.48	29.64	49.44	55.52	23.29	33.26	30.55	30.99	34.43	42.57	83.31	44.23	54.40	56.04	45.94	40.40
FB-OCC [22]★	ResNet101	ICCV’23	43.41	12.10	50.23	32.31	48.55	52.89	31.20	31.25	30.78	32.33	37.06	40.22	83.34	49.27	57.13	59.88	47.67	41.76
Ours★	ResNet101	N/A	44.02	11.96	51.70	29.93	53.52	56.77	30.83	33.17	30.65	29.99	37.76	43.87	83.17	44.52	55.45	58.86	49.52	46.33

Table 2: 3D Semantic Scene Completion performance on SemanticKITTI dataset.

Method	Reference	IoU	mIoU	road	sidewalk	parking	other-ground	building	car	truck	bicycle	motorcycle	other-vehicle	vegetation	trunk	terrain	person	bicyclist	motorcyclist	fence	pole	traf.-sign
LMSCNet [36]	3DV’20	28.61	6.70	40.68	18.22	4.38	0.00	10.31	18.33	0.00	0.00	0.00	0.00	13.66	0.02	20.54	0.00	0.00	0.00	1.21	0.00	0.00
AICNet [17]	CVPR’20	29.59	8.31	43.55	20.55	11.97	0.07	12.94	14.71	4.53	0.00	0.00	0.00	15.37	2.90	28.71	0.00	0.00	0.00	2.52	0.06	0.00
3DSketch [4]	CVPR’20	33.30	7.50	41.32	21.63	0.00	0.00	14.81	18.59	0.00	0.00	0.00	0.00	19.09	0.00	26.40	0.00	0.00	0.00	0.73	0.00	0.00
JS3C-Net [52]	AAAI’21	38.98	10.31	50.49	23.74	11.94	0.07	15.03	24.65	4.41	0.00	0.00	6.15	18.11	4.33	26.86	0.67	0.27	0.00	3.94	3.77	1.45
MonoScene [3]	CVPR’22	36.86	11.08	56.52	26.72	14.27	0.46	14.09	23.26	6.98	0.61	0.45	1.48	17.89	2.81	29.64	1.86	1.20	0.00	5.84	4.14	2.25
TPVFormer [11]	CVPR’23	35.61	11.36	56.50	25.87	20.60	0.85	13.88	23.81	8.08	0.36	0.05	4.35	16.92	2.26	30.38	0.51	0.89	0.00	5.94	3.14	1.52
VoxFormer [18]	CVPR’23	44.02	12.35	54.76	26.35	15.50	0.70	17.65	25.79	5.63	0.59	0.51	3.77	24.39	5.08	29.96	1.78	3.32	0.00	7.64	7.11	4.18
OccFormer [50]	ICCV’23	36.50	13.46	58.84	26.88	19.61	0.31	14.40	25.09	25.53	0.81	1.19	8.52	19.63	3.93	32.63	2.78	2.82	0.00	5.61	4.26	2.86
Symphonies [12]	CVPR’24	41.44	13.44	55.78	26.77	14.57	0.19	18.76	27.23	15.99	1.44	2.28	9.52	24.50	4.32	28.49	3.19	8.09	0.00	6.18	8.99	5.39
Ours	N/A	44.71	13.12	55.13	26.74	18.68	0.65	18.69	28.07	16.43	0.64	0.71	6.03	25.26	4.89	32.47	2.25	2.57	0.00	4.01	3.72	2.36

we employ Adam [14] optimizer with a learning rate of $2e-4$ and weight decay of 0.01. The batch size is 8, and the model is trained for 24 epochs, consuming around 3 days on 8 NVIDIA A100 GPUs.

4.4 Results

3D Occupancy Prediction. In Tab. 1, we provide comparison experiments with other state-of-the-art occupancy prediction methods on Occ3d-nus validation set. The performance of FBOCC [22] relies on open-source code, which we evaluate after ensuring consistency in details (utilizing the same backbone, image resolution, and excluding CBGS [58]) for a fair comparison. Performance for other methods are reported in a series of works [32, 43, 50]. Our approach demonstrates superior performance on mIoU compared to previous methods, particularly excelling in foreground classes such as barriers, cars, and buses, as well as in scene structure classes like manmade and vegetation. This highlights that processing scenes using multiple granularities aligns better with the scene characteristics, enhancing overall expressiveness.

Moreover, we evaluate the efficiency of our approach by comparing it to alternative methods utilizing diverse query forms, as depicted in Tab 3. The results indicate that our approach not only surpasses these methods in terms of performance but also demonstrates significantly reduced memory usage and lower latency compared to dense queries, approaching the levels observed with 2D queries. Clearly, sparse octree queries effectively mitigate computational overhead while ensuring robust performance. Fig. 4 displays qualitative results ob-

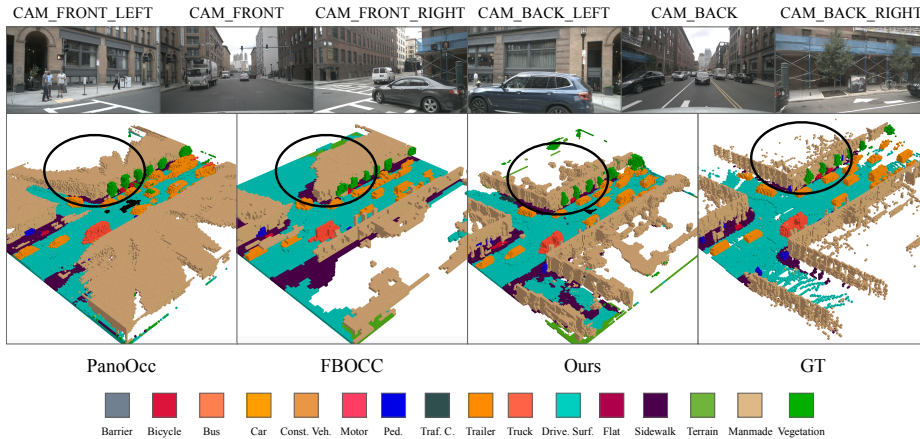


Fig. 4: Qualitative results on Occ3D-nuScenes validation set, where the resolution of the voxel predictions is $200 \times 200 \times 16$.

Table 3: Comparison of query form and efficiency with SOTA methods on the Occ3D-nuScenes (left table) and SemanticKITTI (right table) dataset.

Methods	Query Form	mIoU	Latency	Memory	Methods	Query Form	IoU	mIoU	Latency	Memory
BEVFormer [21]	2D BEV	23.67	302ms	25100M	TPVFormer [11]	2D tri-plane	35.61	11.36	179ms	23000M
TPVFormer [11]	2D tri-plane	28.34	341ms	29000M	OccFormer [56]	3D voxel	36.50	13.46	172ms	22400M
PanoOcc [50]	3D voxel	42.13	502ms	35000M	VoxFormer [18]	3D voxel	44.02	12.35	177ms	23200M
FBOCC [22]	3D voxels & 2D BEV	43.41	463ms	31000M	Symphonics [12]	3D voxel	41.44	13.44	187ms	22000M
Ours	Octree Query	44.02	386ms	26500M	Ours	Octree Query	44.71	13.12	162ms	19000M

tained by our methods and some other methods, illustrating that our approach comprehensively understands the structure of the scene, showcasing superior performance in scene understanding.

3D Semantic Scene Completion. To better evaluate the effectiveness of our approach, we conduct comparative experiments for the Semantic Scene Completion (SSC) task. As demonstrated in Tab 2, we compare our results with those of other SSC methods on the SemanticKITTI validation set. Our model demonstrates a more accurate perception of space due to octree construction and correction, outperforming others in IoU metric for geometry reconstruction. Additionally, for specific semantic classes such as car and vegetation, we achieve superior results, attributed to the enhanced treatment of objects facilitated by multi-granularity modeling. Additionally, Tab 3 also indicates that our method consumes fewer computational resources than other dense query-based methods.

4.5 Ablation Study

In this subsection, we perform ablation studies on the Occ3d-nus validation set to assess the effectiveness of our proposed modules. All the experiments are conducted on the NVIDIA A40 GPU with reducing the input image size to 0.3x. **Effectiveness of Octree Queries.** To validate the superiority of octree queries, we maintained consistent TSA and ICA settings while removing the proposed oc-

Table 4: Ablation experiments of Modules on Occ3d-nuScenes dataset.

	Baseline	Octree Query	Sem.Init.	Iter.Rec.	mIoU	Latency	Memory
(a)	✓				34.17	266 ms	27200M
(b)	✓	✓			34.91	218 ms	18300M
(c)	✓	✓	✓		36.63	214 ms	17900M
(d)	✓	✓		✓	35.88	227 ms	18500M
(e)	✓	✓	✓	✓	37.40	224 ms	18500M

Table 5: Comparison of octree structure quality at different stages.

	Stage	mIoU	
		level 1 to 2	level 2 to 3
(a)	Initialized w/o unbalanced assignment	45.79	33.60
	Initialized w. unbalanced assignment	57.34	51.28
(b)	After the 1st Rectification	60.13	53.95
	After the 2nd Rectification	62.27	56.79

tree structure initialization and rectification modules. This facilitated a comparison with the baseline employing dense queries of size $100 \times 100 \times 16$ (the largest size achievable within memory limitations). As illustrated in Tab. 4 (b), experimental results consistently demonstrate our outperformance, with a notable 0.8 mIoU advantage, despite achieving a memory saving of approximately 9G. This underscores the adeptness of octree prediction in allocating queries with varying granularities to diverse semantic regions. Moreover, the constructed octree queries exhibit adaptability to various object shapes, thereby optimizing the utilization of computational resources.

Effectiveness of Semantic-guided Structure Initialization module. To underscore the significance of the initial octree structure, we exclude the Semantic-guided Octree Initialization module and employ a MLP to predict the octree structure from randomly initialized queries. This results in a 1.7 mIoU performance decrease, highlighting the inaccuracy of structurally predicted information from the initialized query due to the absence of valid information coding. Incorporating semantic priors proves crucial as they enhance the quality of the initialized octree, thereby improving overall model performance. Meanwhile, Tab. 5(a) evaluates the effectiveness of the initial octree structure. We can observe that assigning different initial weights to voxels projected onto different semantic regions directs the initial structure to focus more on the effective areas of the scene, thus improving the quality of the octree structure.

Effectiveness of Iterative Structure Rectification module. We additionally perform an ablation study on the Iterative Structure Rectification module, as shown in Tab. 4(d). The incorporation of this module has led to noticeable improvements in performance. Meanwhile, Tab. 5(b) shows this rectification gradually rectifies areas where structural predictions are incorrect. Consequently, this refinement contributes to the efficiency of octree query expression, positively impacting overall performance.

4.6 More Analysis

In this subsection, we provide more analysis experiments on the Occ3d-nus validation set. All the experiments are conducted on the NVIDIA A40 GPU with reducing the input image size to 0.3x.

Discussion on the depth of octree. Tab. 6 presents experiments on octree depth variations. (a)-(d) show performance with varying 3D query sizes, while (e)-(h) depict octree query performance with different depths and initial resolutions. Comparing (e) to (c) and (f) to (d) reveals our approach achieves comparable performance to dense queries, significantly reducing resource consumption.

Table 6: Ablation for different octree depth on Occ3d-nuScenes *val* set.

	Query Form	Octree Depth	Query Resolution	mIoU	Latency	Memory
(a)	3D voxel	N/A	50×50×4	28.51	129ms	7400M
(b)			50×50×16	31.67	186ms	11600M
(c)			100×100×8	32.21	204ms	17400M
(d)			100×100×16	34.17	266ms	27200M
(e)	Octree Query	2	50×50×4/100×100×8	32.02	182ms	12400M
(f)		3	50×50×4/100×100×8/100×100×16	33.76	207ms	16800M
(g)		4	25×25×2/50×50×4/100×100×8/100×100×16	34.88	193 ms	15800M
(h)		3	50×50×4/100×100×8/200×200×16	37.40	224ms	18500M

Table 7: Ablation for the choice of query selection ratio on Occ3d-nuScenes *val* set.

	Selection Ratio	mIoU	Latency	Memory
(a)	10%, 60%	34.47	191ms	14500M
(b)	15%, 60%	35.01	203ms	16300M
(c)	25%, 50%	36.73	220ms	18000M
(d)	25%, 60%	36.12	255ms	21000M
(e)	20%, 60%	37.40	224ms	18500M

Table 8: Comparison with another octree method.

	mIoU	Latency	Memory
baseline	34.10	266 ms	27200M
OGN [42]	33.39	212 ms	24300M
Ours	37.40	224 ms	18500M

(g) shows that the predetermined octree depth should not be excessive. While reducing memory usage, the imperfect predictions of octree splitting result in accumulated errors, leading to performance degradation as the depth increases.

Discussion on query selection ratio of each level in the octree. In Tab. 7, we present results from maintaining different query ratios in various octree level. Results show that too few or too many queries degrade performance. Inadequate queries result in an imperfect scene representation, especially for detailed regions (a,b vs e). Conversely, excessive queries impact computational efficiency, particularly for coarse-grained regions with empty spaces (c vs d and c,d vs e). Optimizing query numbers based on scene object granularity distribution ensures effective handling of semantic regions at different levels.

Analysis of Various Usage of Octree. As a classic technique, octree is employed in various tasks [7, 15, 41, 42, 46]. Despite differences in addressed problems, we compare our method with OGN [42], which proposes an octree-based upsampling approach. We keep the similar setup in Tab. 4 (b) but substitute the deconvolution decoder with OGN’s octree decoder. Results in Tab. 8 indicate that employing octree solely in the decoder fails to mitigate excessive computational costs and yields sub-optimal performance, mainly due to the high query count during encoding.

5 Conclusions

In conclusion, our paper introduces OctreeOcc, a novel 3D occupancy prediction framework that addresses the limitations of dense-grid representations in understanding 3D scenes. OctreeOcc’s adaptive utilization of octree representations enables the capture of valuable information with variable granularity, catering to objects of diverse sizes and complexities. Our extensive experimental results affirm OctreeOcc’s capability to attain state-of-the-art performance in 3D occupancy prediction while concurrently reducing computational overhead.

References

1. Behley, J., Garbade, M., Milioto, A., Quenzel, J., Behnke, S., Stachniss, C., Gall, J.: Semantickitti: A dataset for semantic scene understanding of lidar sequences. In: Proceedings of the IEEE/CVF international conference on computer vision. pp. 9297–9307 (2019) [10](#)
2. Caesar, H., Bankiti, V., Lang, A.H., Vora, S., Liong, V.E., Xu, Q., Krishnan, A., Pan, Y., Baldan, G., Beijbom, O.: nuscenes: A multimodal dataset for autonomous driving. In: Proceedings of the IEEE/CVF conference on computer vision and pattern recognition. pp. 11621–11631 (2020) [10](#)
3. Cao, A.Q., de Charette, R.: Monoscene: Monocular 3d semantic scene completion. In: Proceedings of the IEEE/CVF Conference on Computer Vision and Pattern Recognition (CVPR). pp. 3991–4001 (June 2022) [3](#), [9](#), [11](#), [20](#)
4. Chen, X., Lin, K.Y., Qian, C., Zeng, G., Li, H.: 3d sketch-aware semantic scene completion via semi-supervised structure prior. In: Proceedings of the IEEE/CVF Conference on Computer Vision and Pattern Recognition. pp. 4193–4202 (2020) [11](#)
5. Dai, J., Qi, H., Xiong, Y., Li, Y., Zhang, G., Hu, H., Wei, Y.: Deformable convolutional networks. In: 2017 IEEE International Conference on Computer Vision (ICCV). pp. 764–773 (2017). <https://doi.org/10.1109/ICCV.2017.89> [10](#)
6. Fu, C., Li, G., Song, R., Gao, W., Liu, S.: Octattention: Octree-based large-scale contexts model for point cloud compression. In: Proceedings of the AAAI Conference on Artificial Intelligence. vol. 36, pp. 625–633 (2022) [4](#)
7. Häne, C., Tulsiani, S., Malik, J.: Hierarchical surface prediction for 3d object reconstruction. In: 2017 International Conference on 3D Vision (3DV). pp. 412–420. IEEE (2017) [4](#), [14](#)
8. Huang, J., Huang, G.: Bevdet4d: Exploit temporal cues in multi-camera 3d object detection. arXiv preprint arXiv:2203.17054 (2022) [11](#)
9. Huang, J., Huang, G., Zhu, Z., Yun, Y., Du, D.: Bevdet: High-performance multi-camera 3d object detection in bird-eye-view. arXiv preprint arXiv:2112.11790 (2021) [1](#), [3](#), [11](#)
10. Huang, Y., Zheng, W., Zhang, B., Zhou, J., Lu, J.: Selfocc: Self-supervised vision-based 3d occupancy prediction (2023) [3](#)
11. Huang, Y., Zheng, W., Zhang, Y., Zhou, J., Lu, J.: Tri-perspective view for vision-based 3d semantic occupancy prediction. In: Proceedings of the IEEE/CVF Conference on Computer Vision and Pattern Recognition. pp. 9223–9232 (2023) [2](#), [3](#), [4](#), [11](#), [12](#)
12. Jiang, H., Cheng, T., Gao, N., Zhang, H., Liu, W., Wang, X.: Symphonize 3d semantic scene completion with contextual instance queries. arXiv preprint arXiv:2306.15670 (2023) [1](#), [3](#), [4](#), [11](#), [12](#)
13. Jiang, Y., Zhang, L., Miao, Z., Zhu, X., Gao, J., Hu, W., Jiang, Y.G.: Polarformer: Multi-camera 3d object detection with polar transformer. In: Proceedings of the AAAI Conference on Artificial Intelligence. vol. 37, pp. 1042–1050 (2023) [3](#)
14. Kingma, D.P., Ba, J.: Adam: A method for stochastic optimization (2017) [11](#)
15. Koneputugodage, C.H., Ben-Shabat, Y., Gould, S.: Octree guided unoriented surface reconstruction. In: Proceedings of the IEEE/CVF Conference on Computer Vision and Pattern Recognition. pp. 16717–16726 (2023) [4](#), [14](#)
16. Lei, H., Akhtar, N., Mian, A.: Octree guided cnn with spherical kernels for 3d point clouds. In: Proceedings of the IEEE/CVF Conference on Computer Vision and Pattern Recognition. pp. 9631–9640 (2019) [4](#)

17. Li, J., Han, K., Wang, P., Liu, Y., Yuan, X.: Anisotropic convolutional networks for 3d semantic scene completion. In: Proceedings of the IEEE/CVF Conference on Computer Vision and Pattern Recognition. pp. 3351–3359 (2020) [11](#)
18. Li, Y., Yu, Z., Choy, C., Xiao, C., Alvarez, J.M., Fidler, S., Feng, C., Anandkumar, A.: Voxformer: Sparse voxel transformer for camera-based 3d semantic scene completion. In: Proceedings of the IEEE/CVF Conference on Computer Vision and Pattern Recognition (CVPR). pp. 9087–9098 (June 2023) [2](#), [3](#), [4](#), [11](#), [12](#)
19. Li, Y., Bao, H., Ge, Z., Yang, J., Sun, J., Li, Z.: Bevstereo: Enhancing depth estimation in multi-view 3d object detection with dynamic temporal stereo (2022) [3](#), [11](#)
20. Li, Y., Ge, Z., Yu, G., Yang, J., Wang, Z., Shi, Y., Sun, J., Li, Z.: Bevdepth: Acquisition of reliable depth for multi-view 3d object detection. In: Proceedings of the AAAI Conference on Artificial Intelligence. vol. 37, pp. 1477–1485 (2023) [3](#)
21. Li, Z., Wang, W., Li, H., Xie, E., Sima, C., Lu, T., Qiao, Y., Dai, J.: Bevformer: Learning bird’s-eye-view representation from multi-camera images via spatiotemporal transformers. In: European conference on computer vision. pp. 1–18. Springer (2022) [3](#), [11](#), [12](#)
22. Li, Z., Yu, Z., Wang, W., Anandkumar, A., Lu, T., Alvarez, J.M.: Fb-bev: Bev representation from forward-backward view transformations. In: Proceedings of the IEEE/CVF International Conference on Computer Vision. pp. 6919–6928 (2023) [1](#), [11](#), [12](#), [22](#)
23. Lin, T.Y., Dollár, P., Girshick, R., He, K., Hariharan, B., Belongie, S.: Feature pyramid networks for object detection. In: Proceedings of the IEEE conference on computer vision and pattern recognition. pp. 2117–2125 (2017) [10](#)
24. Lin, X., Lin, T., Pei, Z., Huang, L., Su, Z.: Sparse4d: Multi-view 3d object detection with sparse spatial-temporal fusion. arXiv preprint arXiv:2211.10581 (2022) [3](#)
25. Liu, Y., Wang, T., Zhang, X., Sun, J.: Petr: Position embedding transformation for multi-view 3d object detection. In: European Conference on Computer Vision. pp. 531–548. Springer (2022) [3](#)
26. Liu, Y., Yan, J., Jia, F., Li, S., Gao, A., Wang, T., Zhang, X.: Petr2: A unified framework for 3d perception from multi-camera images. In: Proceedings of the IEEE/CVF International Conference on Computer Vision. pp. 3262–3272 (2023) [3](#)
27. Liu, Z., Tang, H., Amini, A., Yang, X., Mao, H., Rus, D.L., Han, S.: Bevfusion: Multi-task multi-sensor fusion with unified bird’s-eye view representation. In: 2023 IEEE International Conference on Robotics and Automation (ICRA). pp. 2774–2781. IEEE (2023) [3](#)
28. Ma, Q., Tan, X., Qu, Y., Ma, L., Zhang, Z., Xie, Y.: Cotr: Compact occupancy transformer for vision-based 3d occupancy prediction. arXiv preprint arXiv:2312.01919 (2023) [3](#)
29. Meagher, D.: Geometric modeling using octree encoding. Computer graphics and image processing **19**(2), 129–147 (1982) [2](#), [4](#)
30. Miao, R., Liu, W., Chen, M., Gong, Z., Xu, W., Hu, C., Zhou, S.: Ocdepth: A depth-aware method for 3d semantic scene completion. arXiv preprint arXiv:2302.13540 (2023) [3](#)
31. Ming, Z., Berrio, J.S., Shan, M., Worrall, S.: Inversematrixvt3d: An efficient projection matrix-based approach for 3d occupancy prediction. arXiv preprint arXiv:2401.12422 (2024) [3](#)
32. Pan, M., Liu, J., Zhang, R., Huang, P., Li, X., Liu, L., Zhang, S.: Renderocc: Vision-centric 3d occupancy prediction with 2d rendering supervision (2023) [3](#), [11](#)

33. Park, J., Xu, C., Yang, S., Keutzer, K., Kitani, K., Tomizuka, M., Zhan, W.: Time will tell: New outlooks and a baseline for temporal multi-view 3d object detection. arXiv preprint arXiv:2210.02443 (2022) [3](#)
34. Phillion, J., Fidler, S.: Lift, splat, shoot: Encoding images from arbitrary camera rigs by implicitly unprojecting to 3d. In: Computer Vision–ECCV 2020: 16th European Conference, Glasgow, UK, August 23–28, 2020, Proceedings, Part XIV 16. pp. 194–210. Springer (2020) [3](#)
35. Que, Z., Lu, G., Xu, D.: Voxelcontext-net: An octree based framework for point cloud compression. In: Proceedings of the IEEE/CVF Conference on Computer Vision and Pattern Recognition. pp. 6042–6051 (2021) [4](#)
36. Roldao, L., de Charette, R., Verroust-Blondet, A.: Lmscnet: Lightweight multiscale 3d semantic completion. In: 2020 International Conference on 3D Vision (3DV). pp. 111–119. IEEE (2020) [11](#)
37. Ronneberger, O., Fischer, P., Brox, T.: U-net: Convolutional networks for biomedical image segmentation. In: Medical Image Computing and Computer-Assisted Intervention–MICCAI 2015: 18th International Conference, Munich, Germany, October 5–9, 2015, Proceedings, Part III 18. pp. 234–241. Springer (2015) [7](#)
38. Silva, S., Wannigama, S.B., Ragel, R., Jayatilaka, G.: S2tpvformer: Spatio-temporal tri-perspective view for temporally coherent 3d semantic occupancy prediction. arXiv preprint arXiv:2401.13785 (2024) [3](#)
39. Sima, C., Tong, W., Wang, T., Chen, L., Wu, S., Deng, H., Gu, Y., Lu, L., Luo, P., Lin, D., Li, H.: Scene as occupancy (2023) [3](#), [7](#)
40. Tan, Z., Dong, Z., Zhang, C., Zhang, W., Ji, H., Li, H.: Ovo: Open-vocabulary occupancy. arXiv preprint arXiv:2305.16133 (2023) [1](#), [3](#)
41. Tang, J.H., Chen, W., Yang, J., Wang, B., Liu, S., Yang, B., Gao, L.: Octfield: Hierarchical implicit functions for 3d modeling. arXiv preprint arXiv:2111.01067 (2021) [4](#), [14](#)
42. Tatarchenko, M., Dosovitskiy, A., Brox, T.: Octree generating networks: Efficient convolutional architectures for high-resolution 3d outputs. In: Proceedings of the IEEE international conference on computer vision. pp. 2088–2096 (2017) [4](#), [14](#)
43. Tian, X., Jiang, T., Yun, L., Wang, Y., Wang, Y., Zhao, H.: Occ3d: A large-scale 3d occupancy prediction benchmark for autonomous driving. arXiv preprint arXiv:2304.14365 (2023) [3](#), [10](#), [11](#)
44. Wang, P.S.: Octformer: Octree-based transformers for 3d point clouds. arXiv preprint arXiv:2305.03045 (2023) [4](#)
45. Wang, P.S., Liu, Y., Guo, Y.X., Sun, C.Y., Tong, X.: O-cnn: Octree-based convolutional neural networks for 3d shape analysis. ACM Transactions On Graphics (TOG) **36**(4), 1–11 (2017) [4](#)
46. Wang, P.S., Liu, Y., Tong, X.: Dual octree graph networks for learning adaptive volumetric shape representations. ACM Transactions on Graphics (TOG) **41**(4), 1–15 (2022) [4](#), [14](#)
47. Wang, P.S., Sun, C.Y., Liu, Y., Tong, X.: Adaptive o-cnn: A patch-based deep representation of 3d shapes. ACM Transactions on Graphics (TOG) **37**(6), 1–11 (2018) [4](#)
48. Wang, S., Liu, Y., Wang, T., Li, Y., Zhang, X.: Exploring object-centric temporal modeling for efficient multi-view 3d object detection. arXiv preprint arXiv:2303.11926 (2023) [3](#)
49. Wang, X., Zhu, Z., Xu, W., Zhang, Y., Wei, Y., Chi, X., Ye, Y., Du, D., Lu, J., Wang, X.: Openoccupancy: A large scale benchmark for surrounding semantic occupancy perception. arXiv preprint arXiv:2303.03991 (2023) [3](#)

50. Wang, Y., Chen, Y., Liao, X., Fan, L., Zhang, Z.: Panoocc: Unified occupancy representation for camera-based 3d panoptic segmentation. arXiv preprint arXiv:2306.10013 (2023) [2](#), [3](#), [4](#), [7](#), [11](#), [12](#), [22](#)
51. Wei, Y., Zhao, L., Zheng, W., Zhu, Z., Zhou, J., Lu, J.: Surroundocc: Multi-camera 3d occupancy prediction for autonomous driving. In: Proceedings of the IEEE/CVF International Conference on Computer Vision (ICCV). pp. 21729–21740 (October 2023) [1](#), [3](#), [6](#)
52. Yan, X., Gao, J., Li, J., Zhang, R., Li, Z., Huang, R., Cui, S.: Sparse single sweep lidar point cloud segmentation via learning contextual shape priors from scene completion. In: Proceedings of the AAAI Conference on Artificial Intelligence. vol. 35, pp. 3101–3109 (2021) [11](#)
53. Yang, C., Chen, Y., Tian, H., Tao, C., Zhu, X., Zhang, Z., Huang, G., Li, H., Qiao, Y., Lu, L., et al.: Bevformer v2: Adapting modern image backbones to bird’s-eye-view recognition via perspective supervision. In: Proceedings of the IEEE/CVF Conference on Computer Vision and Pattern Recognition. pp. 17830–17839 (2023) [3](#)
54. Yu, Z., Shu, C., Deng, J., Lu, K., Liu, Z., Yu, J., Yang, D., Li, H., Chen, Y.: Flashocc: Fast and memory-efficient occupancy prediction via channel-to-height plugin. arXiv preprint arXiv:2311.12058 (2023) [3](#)
55. Zhang, H., Yan, X., Bai, D., Gao, J., Wang, P., Liu, B., Cui, S., Li, Z.: Radocc: Learning cross-modality occupancy knowledge through rendering assisted distillation. arXiv preprint arXiv:2312.11829 (2023) [3](#)
56. Zhang, Y., Zhu, Z., Du, D.: Occformer: Dual-path transformer for vision-based 3d semantic occupancy prediction. arXiv preprint arXiv:2304.05316 (2023) [1](#), [3](#), [6](#), [11](#), [12](#)
57. Zhou, C., Zhang, Y., Chen, J., Huang, D.: Octr: Octree-based transformer for 3d object detection. In: Proceedings of the IEEE/CVF Conference on Computer Vision and Pattern Recognition. pp. 5166–5175 (2023) [4](#)
58. Zhu, B., Jiang, Z., Zhou, X., Li, Z., Yu, G.: Class-balanced grouping and sampling for point cloud 3d object detection. arXiv preprint arXiv:1908.09492 (2019) [11](#)
59. Zhu, X., Su, W., Lu, L., Li, B., Wang, X., Dai, J.: Deformable detr: Deformable transformers for end-to-end object detection. arXiv preprint arXiv:2010.04159 (2020) [7](#)

Appendix

A More Details

In this section, we provide detailed explanations of our proposed modules.

For the **Semantic-Guided Octree Initialization**, our approach commences with acquiring semantic segmentation labels for images by projecting occupancy labels onto the surround-view images. Subsequently, a UNet is trained using these labels. The initialization process entails randomly initializing dense queries, where each query’s center point serves as a reference point projected onto the range-view images. If a reference point is projected onto a ground pixel (*i.e.*, driveable surface, other flat, or sidewalk), the probability increases by 0.1. Conversely, if projected onto a background pixel (excluding ground classes), the probability increases by 0.5. Projection onto a foreground pixel increases the probability of requiring a split at that position by 1.0. This process assigns a split probability to each query, and the octree mask is constructed through average pooling, capturing split probabilities at different query levels. After obtaining the octree mask, we designate the top 20% confidence queries as parent queries in level 1, while the remaining queries become Leaf queries and remain unsplit. Moving to level 2, after splitting the parent queries into octants, the top 60% confidence positions are selected as new parent queries, and the remainder as leaf queries. By storing leaf queries at each level, we construct a sparse and multi-granularity octree structure for queries.

In **Iterative Structure Rectification**, at level 1, we retain predictions for the top 10% of positions with confidence. For the remaining positions, a 2-layer MLP is utilized to predict probabilities. These new probabilities are blended with the existing probabilities, with a weight distribution of 60% for the new probabilities and 40% for the old ones. The top 10% of positions with the new probability values are identified as the required splits, shaping the structure of the new level 1. Similarly, at level 2, predictions for the top 30% of positions with confidence are preserved. For positions not in the top 30%, probabilities are predicted using a 2-layer MLP. The new probabilities are computed by merging them with the original probabilities, with an even weight distribution of 50% for each. The top 30% of the new probability values are then selected as the positions necessitating splitting, delineating the structure of the new level 2.

B Octree node index calculation

The hierarchical structure of the octree, particularly the assignment of queries to respective levels, is determined based on the octree mask M_o and the query selection ratio denoted as $\alpha = \{\alpha^1, \alpha^2, \dots, \alpha^{L-1}\}$. These ratios govern the number of subdivisions at each level, thereby defining the hierarchical organization of the octree. The procedure is as follows. For level 1, queries with M_o^l values within the top α^l percentile are identified as candidates for octant subdivision. Subsequently, within octants that have undergone one previous subdivision at the

next level, queries are once again selected based on their values falling within the top α^2 percentile, initiating another round of subdivision. This process continues iteratively until reaching the final level of the octree.

Simultaneously, exploiting the octree structure facilitates the direct conversion of sparse octree queries into dense queries to align with the desired output shape. For a query q_{octree} at level l with the index (a, b, c) , the indexes of its corresponding 8^{L-l} children nodes in level L are determined by $(a \times 2^{L-l} + a_{offset}, b \times 2^{L-l} + b_{offset}, c \times 2^{L-l} + c_{offset})$, where a_{offset} , b_{offset} , and c_{offset} are independent, ranging from 0 to 2^{L-l} . Here, L denotes the depth of the octree. During this process, we allocate the feature of q_{octree} to all of these positions. By iteratively applying this procedure to all queries at each level, we effectively transform Q_{octree} into Q_{dense} .

C More discussion of octree initialization

Given that the FloSP method outlined in MonoScene [3] incorporates a 3D to 2D projection operation, similar to our initialization approach, we additionally adapted this method for comparison. Specifically, we employed FloSP to extract 3D voxel features from 2D image features. Subsequently, we applied a Multi-Layer Perceptron (MLP) to predict the splitting probability of each voxel, replacing the randomly initialized queries used in the original ablation experiments. The results indicate that, although this operation outperforms predictions from randomly initialized queries, it is still constrained by insufficient information, resulting in a decline in overall performance.

Table 9: More ablation of octree initialization

	Initialization Method	mIoU
(a)	Randomly initialised queries	34.91
(b)	Voxel features from FLoSP	35.72
(c)	Semantic-Guided Octree Initialization	37.40

D More Visualization

Fig. 5 shows additional visualizations of proposed OctreeOcc. Evidently, our approach, leveraging the multi-granularity octree modeling, demonstrates superior performance particularly in the categories of truck, bus, and manmade objects.

Fig. 6 illustrates the results of occupancy prediction alongside the corresponding octree structure. For clarity in visualization, we employ distinct colors to represent voxels at various levels of the octree prediction, based on their occupancy status. For improved visualization, only a portion correctly corresponding

to the occupancy prediction is displayed, rather than the entire octree structure, ensuring clarity and focus on the relevant information. Level 3 (voxel size: $0.4\text{m} \times 0.4\text{m} \times 0.4\text{m}$) is depicted in light gray, level 2 (voxel size: $0.8\text{m} \times 0.8\text{m} \times 0.8\text{m}$) in medium gray, and level 1 (voxel size: $1.6\text{m} \times 1.6\text{m} \times 1.6\text{m}$) in dark gray. It's worth noting that level 1 voxels, predominantly situated in free space and within objects, might be less intuitively discernible. Nonetheless, this image underscores the efficacy of octree modeling, which tailors voxel sizes to different semantic regions, enhancing representation accuracy.

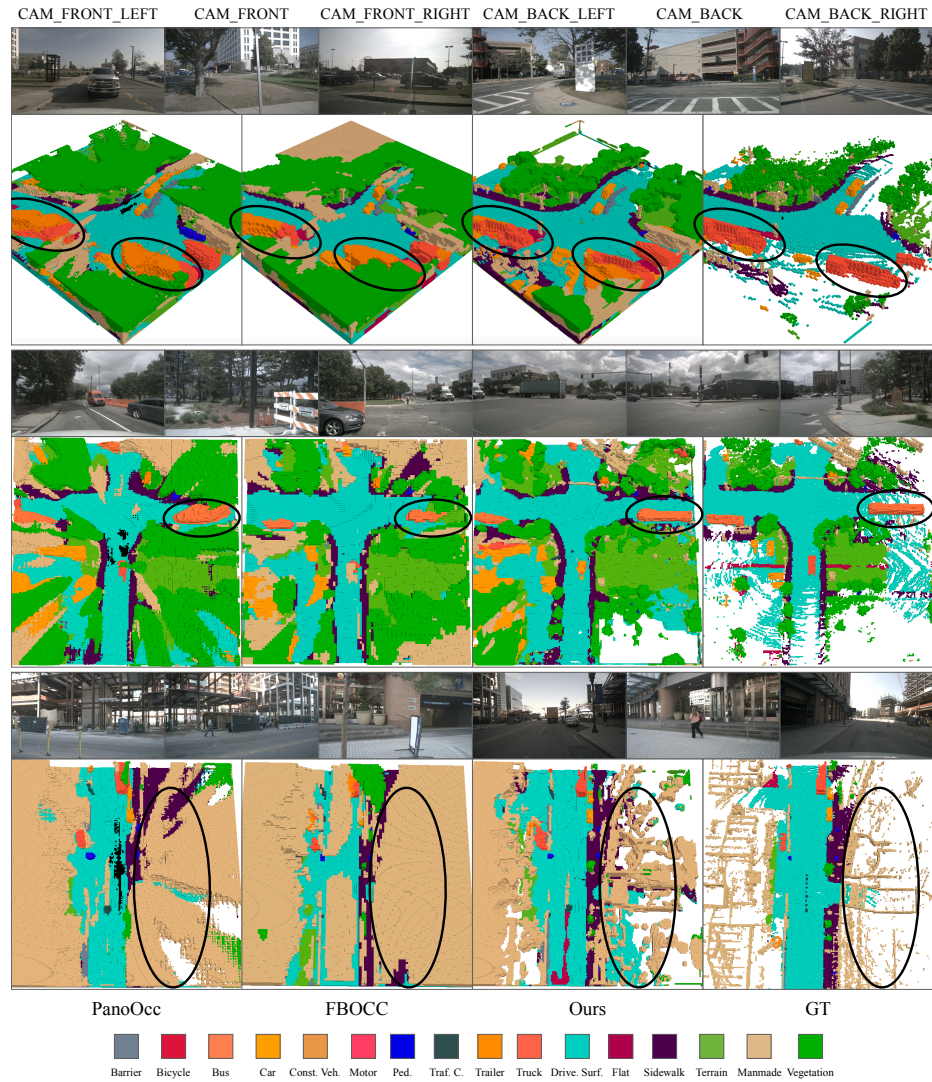


Fig. 5: More visualization on Occ3D-nuScenes validation set. The first row displays input multi-view images, while the second row showcases the occupancy prediction results of PanoOcc [50], FBOCC [22], our methods, and the ground truth.

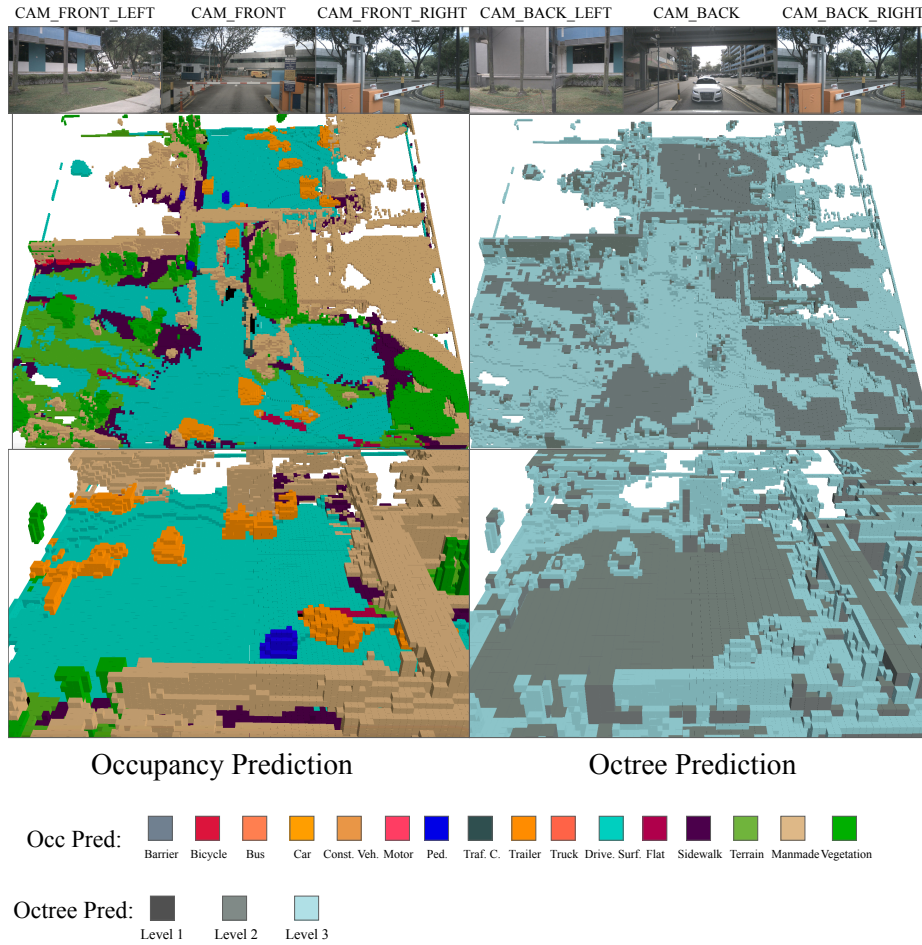


Fig. 6: Visualization of octree structure. The first row displays input multi-view images, while the second and third rows showcase the occupancy prediction results and the corresponding octree structure prediction results.